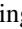






Broadband coplanar-waveguide-based impedance-transformed Josephson parametric amplifierBingcheng Qing ^{1,*} Long B. Nguyen ^{1,2,†} Xinyu Liu ³ Hengjiang Ren,³ William P. Livingston ^{1,2,‡} Noah Goss,^{1,2} Ahmed Hajar,⁴ Trevor Chistolini,¹ Zahra Pedramrazi,^{1,2} David I. Santiago,^{1,2} Jie Luo ³ and Irfan Siddiqi^{1,2}¹*Department of Physics, University of California, Berkeley, California 94720, USA*²*Computational Research Division, Lawrence Berkeley National Laboratory, Berkeley, California 94720, USA*³*Anyon Computing Inc., Emeryville, California 94662, USA*⁴*Graduate Group in Applied Science and Technology, University of California at Berkeley, Berkeley, California, 94720, USA*

(Received 25 October 2023; accepted 8 January 2024; published 22 February 2024)

Quantum-limited Josephson parametric amplifiers play a pivotal role in advancing the field of circuit quantum electrodynamics by enabling the fast and high-fidelity measurement of weak microwave signals. Therefore, it is necessary to develop robust parametric amplifiers with low noise, broad bandwidth, and reduced design complexity for microwave detection. However, current broadband parametric amplifiers either have degraded noise performance or rely on complex designs. Here, we present a device based on the broadband impedance-transformed Josephson parametric amplifier that integrates a hornlike coplanar waveguide transmission line, which significantly decreases the design and fabrication complexity while keeping comparable performance. The device shows an instantaneous bandwidth of 700 (200) MHz for 15 (20) dB gain with an average input saturation power of -110 dBm and near quantum-limited added noise. The operating frequency can be tuned over 1.4 GHz using an external flux bias. We further demonstrate the negligible backaction from our device on a transmon qubit. The amplification performance and simplicity of our device promise its wide adaptation in quantum metrology, quantum communication, and quantum information processing.

DOI: [10.1103/PhysRevResearch.6.L012035](https://doi.org/10.1103/PhysRevResearch.6.L012035)

Introduction. The parametric process facilitates coherent energy transfer among electromagnetic waves by nonlinearities, which enables quantum-limited parametric amplification [1]. Microwave parametric amplification not only improves the readout of solid-state [2–6] and nanomechanical [7] quantum devices, but also becomes increasingly important in emerging technologies such as hybrid quantum systems [8] and axion dark-matter detection [9,10]. It is thus important to develop amplifiers with outstanding performance: low noise, broad bandwidth, and high saturation power. Moreover, for easy adaptation of parametric amplifiers, their design and fabrication should be robust and simple.

In superconducting circuits, parametric amplification is achieved by Josephson parametric amplifiers (JPAs) utilizing multiwave mixing processes in nonlinear superconducting resonators, where Josephson junctions provide the required nonlinearity without introducing dissipation [11,12]. The nonlinear resonator of the JPA is typically coupled to a fixed $50\text{-}\Omega$ embedding environment [13–16], which prevents tuning

its linewidth and saturation power independently, resulting in a trade-off between saturation power and bandwidth [17]. Hence, its bandwidth is inherently limited to 10–50 MHz, and its input saturation power is typically -120 dBm for a nominal gain of 20 dB.

Two strategies have been developed to address this limitation. In the first approach, the nonlinear resonator is unpacked into a nonlinear transmission line by thousands of Josephson junctions, forming a traveling-wave parametric amplifier (TWPA), in which the gain is optimized across a broad range of frequencies [18]. Such a device must satisfy two conditions: (i) the impedance of the amplifier has to match the $50\text{-}\Omega$ environmental impedance, and (ii) the phases of the pump, signal, and idler tones have to match [18]. To fulfill these challenging requirements, 2000 nonlinear unit cells were constructed to form a TWPA with a 20-dB-gain bandwidth over 3 GHz and an input saturation power of -99 dBm [19]. However, TWPA noise processes can be complex [18] and the stringent requirements on the phase matching and the large number of Josephson junctions make the design, calibration, and fabrication difficult for TPWAs [20].

In the second approach, the environmental impedance is engineered to enhance the JPA's coupling, which leads to enhanced bandwidth and saturation power [17]. This has been accomplished by both simple narrowband impedance transformers [21,22] and more complex broadband impedance transformers [17,23,24]. Narrowband impedance transformers constructed using $\lambda/4$ and $\lambda/2$ coplanar waveguides (CPWs) [21,22] or Chebyshev matching networks [25] enhance the JPA's bandwidth to 300 or 500 MHz with fixed operating

*bc.qing@berkeley.edu

†longbnguyen@berkeley.edu

‡Present address: Google Quantum AI, Mountain View, CA 94043, USA.

Published by the American Physical Society under the terms of the [Creative Commons Attribution 4.0 International license](https://creativecommons.org/licenses/by/4.0/). Further distribution of this work must maintain attribution to the author(s) and the published article's title, journal citation, and DOI.

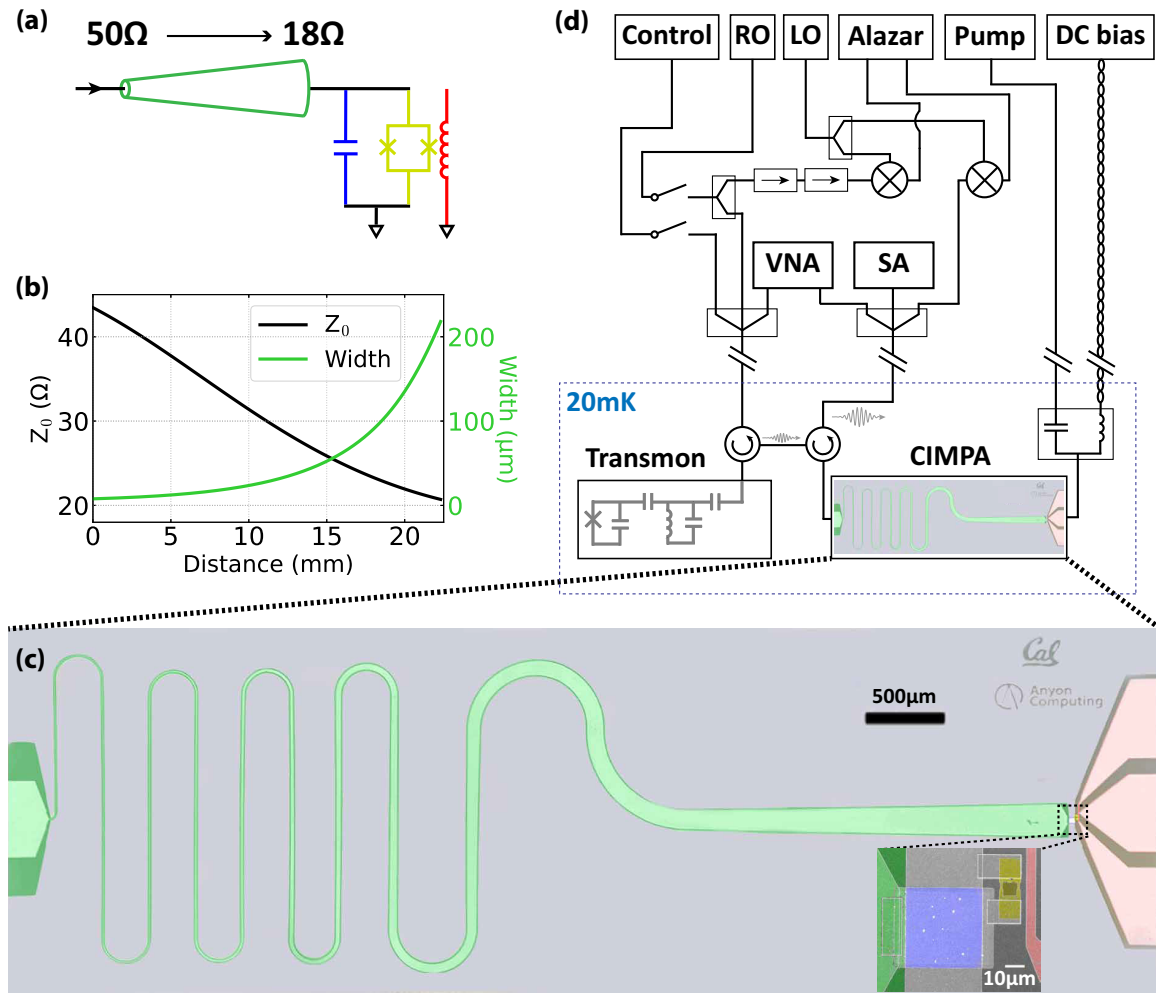


FIG. 1. Experimental concept. (a) Electrical circuit depiction of the CIMPA. The nonlinear resonator on the right side is constructed by shunting a SQUID (yellow) with a capacitor (blue). The structure is galvanically coupled to a Klopfenstein taper (green) on the left and inductively coupled to a flux line (red) on the right. (b) Parameters of the hornlike CPW impedance transformer, showing decreasing characteristic impedance Z_0 along the CPW as its center-trace width becomes wider, transforming from 50Ω at the left end to 18Ω at the right end. One should notice that the characteristic impedance of the hornlike CPW is not exactly equal to 50Ω and 18Ω on the two ends because of the nature of the Klopfenstein taper [26]. (c) False-color micrograph of the device with the nonlinear resonator shown in the inset. From left to right are the hornlike CPW taper (green), the parallel plate capacitor (blue) and SQUID (yellow) forming the resonator, and the on-chip flux line (red). (d) Simplified diagram of the measurement apparatus (details in the Supplemental Material [27]). A transmon qubit is utilized to calibrate the input power and detect possible backaction from the CIMPA.

frequency, respectively. On the other hand, JPAs with broadband impedance transformers following Klopfenstein [17,23] or Ruthroff [24] taper designs have instantaneous bandwidth in the range of 600–700 MHz and allow tunable operating frequencies, but their current implementations either require multilayer fabrication with lossy dielectrics [17,24] or careful simulation and calibration of finely patterned interdigitated capacitors [23]. These requirements increase the complexity of these amplifiers’ design, calibration, and fabrication.

In this Letter, we present a broadband CPW-based impedance-transformed parametric amplifier (CIMPA) design and showcase its performance. By reducing the technical requirements of the Klopfenstein taper, we can implement it using a single hornlike CPW, which keeps the broadband behavior while maintaining the simplicity of the design and fabrication [27]. The hornlike CPW structure allows us to leverage streamlined rf design tools [28] and minimize the

complexity of simulating and fabricating the impedance transformer, and the feature size of the hornlike CPW is well within the scope of the optical lithography technique. Notably, the CIMPA performs as well as the other impedance-transformed parametric amplifiers (IMPAs) despite such simplicity. The amplifier displays an instantaneous bandwidth of 700 (200) MHz for 15 (20) dB gain, a 1.4 GHz flux-tunable bandwidth, a saturation input power of approximately -110 dBm, and no significant backaction on the qubit.

Device Concept. The CIMPA is constructed from three basic building blocks, as depicted by the circuit diagram in Fig. 1(a). The core component of the device is a nonlinear parallel inductor-capacitor (LC) resonator that facilitates the necessary parametric process through which amplification occurs. It consists of a superconducting quantum interference device (SQUID, yellow) shunted by a capacitor (blue). On the right-hand side, it is inductively coupled to a flux line (red)

that allows *in situ* tuning of the resonator frequency and rf flux pumping [14,22]. On the left-hand side, it is galvanically connected to an impedance transformer (green) that is central to improving its bandwidth and dynamic range.

The CIMPA operates as follows. When an rf microwave pump is applied to the nonlinear resonator via the flux line at approximately twice its resonant frequency, $\omega_p \approx 2\omega_0$, we can apply the rotating wave approximation (RWA) in the frame rotating at the signal frequency $\omega_s \approx \omega_0$ and write the dressed Hamiltonian as [27,29]

$$\hat{\mathcal{H}}/\hbar = \Delta \hat{a}^\dagger \hat{a} + \lambda(\hat{a}^{\dagger 2} + \hat{a}^2) + \hat{O}(\hat{a}^4), \quad (1)$$

where \hat{a} (\hat{a}^\dagger) is the bosonic annihilation (creation) operator associated with the resonator, and $\Delta = \omega_p/2 - \omega_0 \sim 0$. $\lambda = \delta f E_{J,\text{eff}} \sqrt{\sin(F) \tan(F) E_c / (8E_{J,\text{eff}})}$ originates from the modulation of the external flux by the pump (details in Supplemental Material [27]), where δf is the modulation depth, F is the dc flux bias, and E_c , $E_{J,\text{eff}}$ are the capacitive energy and effective Josephson energy of the CIMPA. If the circuit is coupled to the environment with strength κ , its input-output equation of motion is given by

$$\dot{\hat{a}} = \frac{i}{\hbar} [\hat{\mathcal{H}}, \hat{a}] - \frac{\kappa}{2} \hat{a} + \sqrt{\kappa} \hat{a}_{\text{in}} = -2i\lambda \hat{a}^\dagger - \frac{\kappa}{2} \hat{a} + \sqrt{\kappa} \hat{a}_{\text{in}}, \quad (2)$$

where \hat{a}_{in} and \hat{a}_{out} are the bosonic operators associated with incoming and outgoing signals. We then proceed to define $\bar{a}[\omega] = \int_{-\infty}^{\infty} dt e^{i\omega t} \hat{a}(t)$ as the frequency-domain bosonic annihilation operator and $\kappa[\omega]$ as the frequency-dependent decay rate, then use the boundary condition $\sqrt{\kappa[\omega]} \bar{a}[\omega] = \bar{a}_{\text{in}}[\omega] + \bar{a}_{\text{out}}[\omega]$ to obtain

$$\begin{aligned} \bar{a}_{\text{out}}[\omega] &= \left[\kappa[\omega] \frac{\kappa[\omega]/2 - i\omega}{(\kappa[\omega]/2 - i\omega)^2 - 4|\lambda|^2} - 1 \right] \bar{a}_{\text{in}}[\omega] \\ &\quad + \left[\frac{-2i\kappa[\omega]\lambda}{(\kappa[\omega]/2 - i\omega)^2 - 4|\lambda|^2} \right] \bar{a}_{\text{in}}^\dagger[-\omega] \\ &= \mathcal{G}(\omega) \bar{a}_{\text{in}}[\omega] + \mathcal{I}(-\omega) \bar{a}_{\text{in}}^\dagger[-\omega], \end{aligned} \quad (3)$$

from which the gain is define, $G(\omega) = |\mathcal{G}(\omega)|^2$.

For a suitable value of λ , the denominator in Eq. (3) approaches zero, resulting in a large signal gain that remains at finite values in practice because of higher-order terms that are not included in Eq. (1) [30]. In addition, large signal power may lead to an ac Stark shift and pump power depletion, thereby decreasing the effective gain [30]. The incoming signal power associated with a gain drop of 1 dB is defined as the input saturation power or, alternatively, the 1-dB compression point.

Importantly, Eq. (3) shows that the amplifier's bandwidth is determined by the coupling strength κ , and thereby can be improved by enhancing the coupling between the resonator and the signal. For the circuit shown in Fig. 1(a), this coupling rate is given as $\kappa = \text{Re}[(CZ_{\text{in}})^{-1}]$, while the saturation power is $P_{\text{sat}} \sim C/Z_{\text{in}}$ [17], where Z_{in} is the input impedance of the coupled environment. Z_{in} is similar to the characteristic impedance of the transmission line Z_0 , but modified by the reflection coefficient S_{11} due to the standing waves from reflection. The input impedance is given by $Z_{\text{in}} = Z_0(1 + S_{11})/(1 - S_{11})$ (details in Supplemental Material [26,27]). Thus, by engineering Z_0 and, accordingly, Z_{in} ,

one can increase both the bandwidth and the dynamic range of the amplifier. Since the signals must come through a nominal 50- Ω transmission line before and after interacting with the amplifier, an impedance transformer is necessary for enhanced coupling, shown on the left-hand side of Fig. 1(a).

Previously, this idea was realized using a broadband impedance transformer based on the Klopfenstein taper with a characteristic impedance ranging from 50 Ω at one end to 15 Ω at the other end, and a maximum return loss of -20 dB above the cutoff frequency [17,23]. These stringent requirements may lead to sophisticated designs that are associated with tedious simulation procedures and complex nanofabrication processes. Alternatively, a combination of quarter-wavelength and half-wavelength CPW resonators can be used [21], with the setback of having a narrower bandwidth, thereby negating the flux-tunable advantage of the SQUID.

Our design unifies the advantages of these two approaches by relaxing the condition on maximum return loss to -10 dB. This allows us to engineer a hornlike CPW transformer with characteristic impedance varying from 50 Ω to 18 Ω following the Klopfenstein taper profile [Fig. 1(b)]. The hornlike CPW impedance transformer is designed by fixing its gap to 3 μm and varying the center-trace width from 7.8 to 218 μm . The single CPW structure can be simulated using simple rf design suites such as TX-LINE [28], and its dimensions are compatible with single-layer photolithography and reactive-ion etching techniques (details in Supplemental Material [27]). As a result, this approach significantly reduces the complexity overhead in both design and fabrication, which is reflected by the simple construction of our device shown in Fig. 1(c).

Device Characterization. The CIMPA is wire bonded to a printed circuit board (PCB) and packaged using a copper box. The device is then attached to the mixing chamber stage of a dilution fridge operating at 20 mK. It is connected to room-temperature microwave apparatus as shown in Fig. 1(d). A transmon qubit is integrated into the measurement setup to calibrate the signal power and detect possible backaction from the parametric process. Two QuinStar 4–8 GHz cryogenic circulators are used to route the signals, and the signals leaving the transmon are amplified

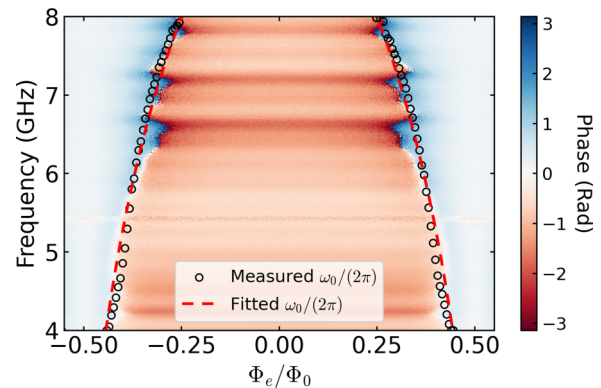


FIG. 2. CIMPA's spectrum. Reflectometry spectroscopy performed using a VNA shows phase twists across the SQUID's resonant frequencies. Repeating the measurement at various flux biases yields the CIMPA's characteristic frequency spectrum, which fits the relation given by Eq. (4) with excellent agreement.

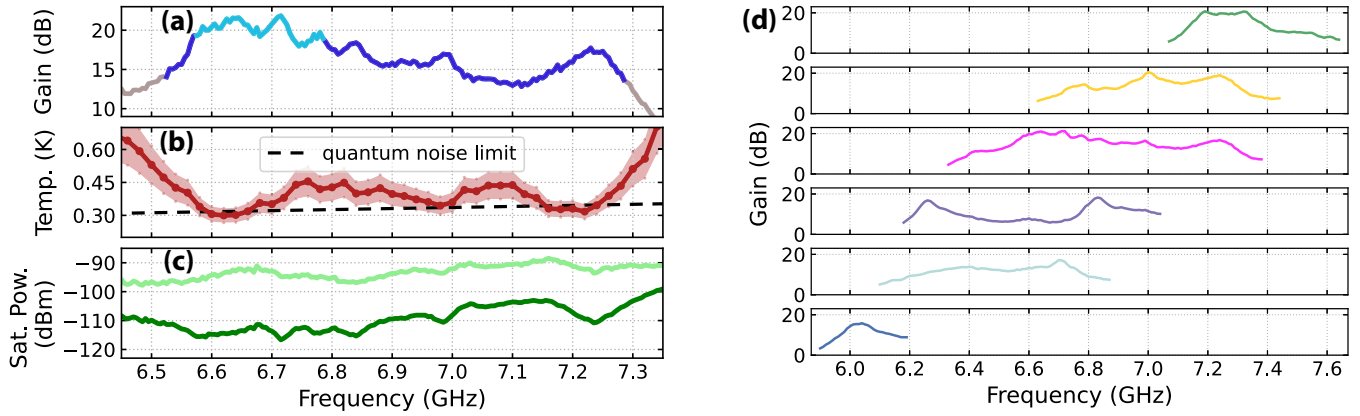


FIG. 3. CIMPA's performance. (a) Instantaneous signal gain, where the 20-dB-gain range is highlighted in cyan and 15-dB-gain range is highlighted in blue, (b) noise temperature, and (c) input saturation power (dark green) and output saturation power (light green) of the CIMPA operated at $\Phi_e/\Phi_0 = 0.3$ and $\omega_p = 2\pi \times 13.41$ GHz. (d) Signal gain at different CIMPA frequencies tuned by varying Φ_e .

by the CIMPA and a high-electron-mobility transistor amplifier (HEMT) (wiring details are given in the Supplemental Material [27]).

In the first step, we extract the parameters of the nonlinear resonator by measuring the small-signal linear response of the device using a vector network analyzer (VNA). As the probe signal goes through $\omega_0/(2\pi)$, the reflected signal phase is twisted, indicating a resonant condition, and the resonant frequency is extracted by fitting the reflection spectrum [31]. When we adjust the external flux bias Φ_e of the SQUID, the resonant frequency changes according to

$$\omega_0 = \{C[L_{J,\text{eff}}|\cos(\pi\Phi_e/\Phi_0)|^{-1} + L_{\text{geo}}]\}^{-1/2}, \quad (4)$$

where L_{geo} is the parasitic geometric inductance originating from the leads, L_{eff} is the effective inductance of the SQUID at zero flux, and Φ_0 is the magnetic flux quantum. Measuring the phase response at each flux point gives us the spectrum shown in Fig. 2. By fitting the measured spectrum, we extract the following parameters: $L_{J,\text{eff}} = 69$ pH, $C = 4$ pF, and $L_{\text{geo}} < 4$ pH. The spectrum also allows us to estimate the asymmetry of the SQUID to be less than 1%.

We proceed to characterize the CIMPA's gain profile, noise performance, and dynamic range. We set the external flux bias to $\Phi_e = 0.3\Phi_0$ and apply a microwave pump tone at frequency $\omega_p/(2\pi) = 13.41$ GHz with 3.41 dBm power outside the fridge. We measure the microwave response using the VNA, observing over 20 (15) dB gain over a 200-(700)-MHz bandwidth [Fig. 3(a)]. Such a high increase in the bandwidth cannot be explained solely by the increased resonator linewidth [17]. As discussed in Ref. [17], the weak frequency dependence of Z_{in} due to possible impedance mismatch strongly assists the enhancement of the bandwidth, but it hinders the quantitative comparison between the theory and experiments without the careful calibration of the impedance of the measurement chain [27]. A qualitative comparison with the calculated gain performance is presented in the Supplemental Material [27].

The noise performance of the device can be characterized via the signal-to-noise ratio (SNR) improvement $\text{SNR}_{\text{imprv}}$ measured by a spectrum analyzer (SA) [17,19,21,32]. In an

amplification chain consisting of a CIMPA and a HEMT, the SNR improvement due to the CIMPA is given as

$$\text{SNR}_{\text{imprv}} = \left(\frac{T_{\text{CIMPA}}}{T_{\text{HEMT}}} + \frac{1}{G} \right)^{-1}, \quad (5)$$

where T_{CIMPA} and T_{HEMT} indicate the noise temperatures of the CIMPA and the HEMT, respectively. The extracted noise temperature with $T_{\text{HEMT}} = 2.3 - 2.9$ K is shown in Fig. 3(b), which approaches the quantum noise limit. The uncertainty here originates from the estimated T_{HEMT} range. The device approaches the quantum noise limit over the 700 MHz range, and the noise increase beyond this range is mainly because the CIMPA's gain is not large enough to compensate for the noise at the HEMT.

Presently, we characterize the saturation power of the device as follows. First, the relation between the actual signal power going into the CIMPA and the power set on the VNA must be established. By measuring the ac Stark shift and measurement-induced dephasing of the transmon qubit at various VNA powers, we can calibrate the cable attenuation [19] (calibration details in Supplemental Material [27]). Then, we gradually increase the power until the gain falls off by 1 dB and convert this using the established attenuation. The result in Fig. 3(c) shows an average input 1-dB compression point of approximately -110 dBm. Compared with the input saturation power of simple JPAs coupled to a 50Ω environment (with $Q \approx 15$), which is less than -120 dBm [14,17,24], our saturation power is increased by around 10 dB. This can be explained by the reduction in the environment's input impedance in our design (with $Q \approx 4$), as $P_{\text{sat}} \sim C/Z_{\text{in}}$ [17].

In addition to the instantaneous bandwidth, we can flux tune the device and operate it at other frequencies. To showcase this capability, we calibrate the CIMPA's parameters at five different external flux points corresponding to a frequency range of 1.4 GHz, and we then characterize the gain performance of the device across this broad range. Figure 3(d) shows that the combination of the engineered broadband impedance transformer and the inherent flux tunability allows the device to amplify signals with frequency ranging from 6 to 7.4 GHz and at least 15 dB of maximum gain.

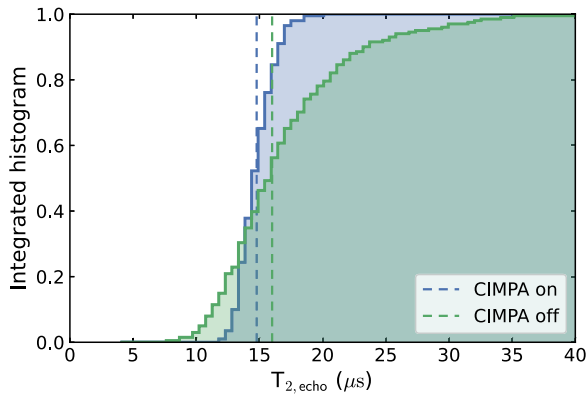


FIG. 4. Transmon's coherence time statistics for CIMPA on (pumped) and off (unpumped), with the mean values equal to 14.78 and 16 μs , and the standard deviations equal to 1.41 and 5.45 μs , respectively. The statistics consist of 201 individual measurements in each setting.

Importantly, possible backaction from the parametric process can undermine the integration of an amplifier into a qubit measurement setup. For example, spurious microwave radiation from the CIMPA can populate the readout resonator connected to the qubit, leading to photon-noise dephasing [33,34]. To investigate the possible backaction of the CIMPA device, we measure the echo time $T_{2,\text{echo}}$ of the qubit with and without amplification. To turn off the CIMPA, we remove the pump tone and flux tune its frequency away from the qubit's readout resonator, such that the amplifier acts as a passive mirror. When the CIMPA is turned on, it provides a gain of 21 dB for the readout signal frequency at 6.633 GHz. The $T_{2,\text{echo}}$ measurement is repeated continuously over 201 iterations in each setting to provide reliable statistics despite

temporal fluctuations. We attribute the wider fluctuation range associated with the measurement when the CIMPA is off to the approximately 10-times-longer data acquisition time. As shown in Fig. 4, there is no significant degradation of the qubit's coherence time beyond random fluctuation when the CIMPA is operated.

Summary and discussion. In conclusion, we show that the CIMPA's design and fabrication is as simple as the JPA's, yet its performance is comparable to earlier IMPA implementations. Therefore, it fills the technological gap between JPAs and TWPAs, with potential applications ranging from qubit readout to axion dark-matter detection. Compared to typical TWPAs, the CIMPA device reported here has a narrower bandwidth and lower dynamic range. However, we note that on one hand, a majority of quantum experiments do not require a 3-GHz bandwidth, and on the other hand, we can integrate SQUID arrays [25,35] or superconducting nonlinear asymmetric inductive elements (SNAIL) [20] into the CIMPA design to increase its power-handling capability.

Acknowledgments. We thank Larry Chen and Kan-Heng Lee for providing the transmon sample. This work was supported by the Quantum Testbed Program of the Advanced Scientific Computing Research Division, Office of Science of the U.S. Department of Energy under Contract No. DE-AC02-05CH11231.

J.L. and B.Q. conceived and organized the project. X.L., B.Q., and H.R. fabricated the device. B.Q., L.B.N., and X.L. performed the measurement and acquired the data. B.Q. analyzed the results. N.G. assisted with the measurement apparatus. A.H. and Z.P. assisted with the cryogenic setup. W.P.L. and T.C. assisted with initiating the project. H.R., J.L., D.I.S., and I.F. supervised the effort. B.Q. and L.B.N. wrote the manuscript with input from all authors.

X.L., H.R., and J.L. are employees of Anyon Computing, Inc.

-
- [1] C. M. Caves, Quantum limits on noise in linear amplifiers, *Phys. Rev. D* **26**, 1817 (1982).
 - [2] A. Blais, A. L. Grimsmo, S. M. Girvin, and A. Wallraff, Circuit quantum electrodynamics, *Rev. Mod. Phys.* **93**, 025005 (2021).
 - [3] G. Burkard, T. D. Ladd, A. Pan, J. M. Nichol, and J. R. Petta, Semiconductor spin qubits, *Rev. Mod. Phys.* **95**, 025003 (2023).
 - [4] R. Vijay, D. H. Slichter, and I. Siddiqi, Observation of quantum jumps in a superconducting artificial atom, *Phys. Rev. Lett.* **106**, 110502 (2011).
 - [5] M. Hatridge, S. Shankar, M. Mirrahimi, F. Schackert, K. Geerlings, T. Brecht, K. M. Sliwa, B. Abdo, L. Frunzio, S. M. Girvin *et al.*, Quantum back-action of an individual variable-strength measurement, *Science* **339**, 178 (2013).
 - [6] F. Arute, K. Arya, R. Babbush, D. Bacon, J. C. Bardin, R. Barends, R. Biswas, S. Boixo, F. G. S. L. Brandao, D. A. Buell *et al.*, Quantum supremacy using a programmable superconducting processor, *Nature (London)* **574**, 505 (2019).
 - [7] B. Arash, J.-W. Jiang, and T. Rabczuk, A review on nanomechanical resonators and their applications in sensors and molecular transportation, *Appl. Phys. Rev.* **2**, 021301 (2015).
 - [8] A. A. Clerk, K. W. Lehnert, P. Bertet, J. R. Petta, and Y. Nakamura, Hybrid quantum systems with circuit quantum electrodynamics, *Nat. Phys.* **16**, 257 (2020).
 - [9] A. Caldwell, G. Dvali, B. Majorovits, A. Millar, G. Raffelt, J. Redondo, O. Reimann, F. Simon, and F. Steffen (MADMAX Working Group), Dielectric haloscopes: A new way to detect axion dark matter, *Phys. Rev. Lett.* **118**, 091801 (2017).
 - [10] T. Nitta, T. Braine, N. Du, M. Guzzetti, C. Hanretty, G. Leum, L. J. Rosenberg, G. Rybka, J. Sinnis, J. Clarke, I. Siddiqi, M. H. Awida, A. S. Chou, M. Hollister, S. Knirck, A. Sonnenschein, W. Wester, J. R. Gleason, A. T. Hipp, P. Sikivie *et al.* (ADMX Collaboration), Search for a dark-matter-induced cosmic axion background with ADMX, *Phys. Rev. Lett.* **131**, 101002 (2023).
 - [11] A. Roy and M. Devoret, Introduction to parametric amplification of quantum signals with Josephson circuits, *C. R. Phys.* **17**, 740 (2016).
 - [12] V. E. Manucharyan, E. Boaknin, M. Metcalfe, R. Vijay, I. Siddiqi, and M. Devoret, Microwave bifurcation of a Josephson junction: Embedding-circuit requirements, *Phys. Rev. B* **76**, 014524 (2007).

- [13] M. A. Castellanos-Beltran and K. W. Lehnert, Widely tunable parametric amplifier based on a superconducting quantum interference device array resonator, *Appl. Phys. Lett.* **91**, 083509 (2007).
- [14] T. Yamamoto, K. Inomata, M. Watanabe, K. Matsuba, T. Miyazaki, W. D. Oliver, Y. Nakamura, and J. S. Tsai, Flux-driven Josephson parametric amplifier, *Appl. Phys. Lett.* **93**, 042510 (2008).
- [15] N. Bergeal, F. Schackert, M. Metcalfe, R. Vijay, V. E. Manucharyan, L. Frunzio, D. E. Prober, R. J. Schoelkopf, S. M. Girvin, and M. H. Devoret, Phase-preserving amplification near the quantum limit with a Josephson ring modulator, *Nature (London)* **465**, 64 (2010).
- [16] M. Hatridge, R. Vijay, D. H. Slichter, J. Clarke, and I. Siddiqi, Dispersive magnetometry with a quantum limited SQUID parametric amplifier, *Phys. Rev. B* **83**, 134501 (2011).
- [17] J. Y. Mutus, T. C. White, R. Barends, Y. Chen, Z. Chen, B. Chiaro, A. Dunsworth, E. Jeffrey, J. Kelly, A. Megrant *et al.*, Strong environmental coupling in a Josephson parametric amplifier, *Appl. Phys. Lett.* **104**, 263513 (2014).
- [18] M. Esposito, A. Ranadive, L. Planat, and N. Roch, Perspective on traveling wave microwave parametric amplifiers, *Appl. Phys. Lett.* **119**, 120501 (2021).
- [19] C. Macklin, K. O'Brien, D. Hover, M. E. Schwartz, V. Bolkhovskiy, X. Zhang, W. D. Oliver, and I. Siddiqi, A near-quantum-limited Josephson traveling-wave parametric amplifier, *Science* **350**, 307 (2015).
- [20] D. Ezenkova, D. Moskalev, N. Smirnov, A. Ivanov, A. Matanin, V. Polozov, V. Echeistov, E. Malevannaya, A. Samoylov, E. Zikiy *et al.*, Broadband SNAIL parametric amplifier with microstrip impedance transformer, *Appl. Phys. Lett.* **121**, 232601 (2022).
- [21] T. Roy, S. Kundu, M. Chand, A. M. Vadiraj, A. Ranadive, N. Nehra, M. P. Patankar, J. Aumentado, A. A. Clerk, and R. Vijay, Broadband parametric amplification with impedance engineering: Beyond the gain-bandwidth product, *Appl. Phys. Lett.* **107**, 262601 (2015).
- [22] J. Grebel, A. Bienfait, É. Dumur, H.-S. Chang, M.-H. Chou, C. R. Conner, G. A. Peairs, R. G. Povey, Y. P. Zhong, and A. N. Cleland, Flux-pumped impedance-engineered broadband Josephson parametric amplifier, *Appl. Phys. Lett.* **118**, 142601 (2021).
- [23] Y. Lu, W. Xu, Q. Zuo, J. Pan, X. Wei, J. Jiang, Z. Li, K. Zhang, T. Guo, S. Wang *et al.*, Broadband Josephson parametric amplifier using lumped-element transmission line impedance matching architecture, *Appl. Phys. Lett.* **120**, 082601 (2022).
- [24] L. Ranzani, G. Ribeill, B. Hassick, and K. C. Fong, Wideband Josephson parametric amplifier with integrated transmission line transformer, *2022 IEEE International Conference on Quantum Computing and Engineering (QCE)* (IEEE, Piscataway, NJ, 2022), pp. 314–319.
- [25] R. Kaufman, T. White, M. I. Dykman, A. Iorio, G. Stirling, S. Hong, A. Opremcak, A. Bengtsson, L. Faoro, J. C. Bardin *et al.*, Josephson parametric amplifier with Chebyshev gain profile and high saturation, [arXiv:2305.17816](https://arxiv.org/abs/2305.17816).
- [26] D. M. Pozar, *Microwave Engineering* (Wiley, New York, 2011).
- [27] See Supplemental Material at <http://link.aps.org/supplemental/10.1103/PhysRevResearch.6.L012035> for detailed device parameters, fabrication processes, measurement calibration, Hamiltonian analysis, and stability analysis.
- [28] R. N. Simons, *Coplanar Waveguide Circuits, Components, and Systems* (Wiley, New York, 2004).
- [29] A. W. Eddins, *Superconducting Circuits for Quantum Metrology with Nonclassical Light* (University of California, Berkeley, 2017).
- [30] S. Boutin, D. M. Toyli, A. V. Venkatramani, A. W. Eddins, I. Siddiqi, and A. Blais, Effect of higher-order nonlinearities on amplification and squeezing in Josephson parametric amplifiers, *Phys. Rev. Appl.* **8**, 054030 (2017).
- [31] W. Livingston, *Continuous Feedback on Quantum Superconducting Circuits* (University of California, Berkeley, 2021).
- [32] J. Aumentado, Superconducting parametric amplifiers: The state of the art in Josephson parametric amplifiers, *IEEE Microwave* **21**, 45 (2020).
- [33] J. Gambetta, A. Blais, D. I. Schuster, A. Wallraff, L. Frunzio, J. Majer, M. H. Devoret, S. M. Girvin, and R. J. Schoelkopf, Qubit-photon interactions in a cavity: Measurement-induced dephasing and number splitting, *Phys. Rev. A* **74**, 042318 (2006).
- [34] W. F. Kindel, M. D. Schroer, and K. W. Lehnert, Generation and efficient measurement of single photons from fixed-frequency superconducting qubits, *Phys. Rev. A* **93**, 033817 (2016).
- [35] T. White, A. Opremcak, G. Sterling, A. Korotkov, D. Sank, R. Acharya, M. Ansmann, F. Arute, K. Arya, J. C. Bardin *et al.*, Readout of a quantum processor with high dynamic range Josephson parametric amplifiers, *Appl. Phys. Lett.* **122**, 014001 (2023).